High-fidelity 3D Printing using Flashing Photopolymerization

Shangting You[1], Pengrui Wang[2], Jacob Schimelman[1], Henry H. Hwang[1], Shaochen Chen[1,2,3]*

[1]Department of NanoEngineering, University of California San Diego, 9500 Gilman Drive, La Jolla, California, 92093, USA.

[2]Materials Science and Engineering Program, University of California San Diego, 9500 Gilman Drive, La Jolla, California, 92093, USA.

[3]Chemical Engineering Program, University of California San Diego, 9500 Gilman Drive, La Jolla, California, 92093, USA.

* chen168@eng.ucsd.edu

KEYWORDS: 3D printing; flashing photopolymerization; chemical kinetics; light scattering

ABSTRACT: Photopolymerization-based 3D printing has emerged as a promising technique to fabricate 3D structures. However, during the printing process, polymerized materials such as hydrogels often become highly light-scattering, thus perturbing incident light distribution and thereby deteriorating the final print resolution. To overcome this scattering-induced resolution deterioration, we developed a novel method termed flashing photopolymerization (FPP). Our FPP approach is informed by the fundamental kinetics of photopolymerization reactions, where light exposure is delivered in millisecond-scale 'flashes', as opposed to continuous light exposure. During the period of flash exposure, the prepolymer material negligibly scatters light as

photoinitiation occurs. As the material polymerizes and subsequently opacifies in absence of light, the exposure pattern is not perturbed by scattering. Compared to the conventional use of a continuous wave (CW) light source, the FPP fabrication resolution is improved. FPP also shows little dependency on the exposure, thus minimizing trial-and-error type optimization. Using FPP, we demonstrate its use in generating high-fidelity 3D printed constructs.

1. Introduction

Photopolymerization-based 3D printing techniques [1–5] are powerful tools in 3D freeform structure fabrication–they are able to fabricate micro- and nano- scale complex geometries that would otherwise be challenging to achieve with traditional fabrication methods, such as machining or molding. Among the various types of photopolymerization-based 3D printing techniques, light-projection-based 3D printing methods, such as continuous liquid interface production (CLIP),[1] projection micro-stereolithography (PμSL),[2] and dynamic optical projection stereolithography (DOPsL) [6] employ a digital light processing (DLP) technique to project arbitrary patterns onto a prepolymer solution, achieving both a fine resolution and fast fabrication speed.[7] Photopolymerization-based 3D printing has found numerous promising applications in consumer products as well as biomedical engineering such as implantation,[8] imaging,[9] tissue culture,[10,11] drug delivery,[12] and so on.[13–16] However, despite these successful demonstrations of 3D polymeric structure fabrication, this technique faces significant challenges to fabricate functional devices with micron-sized features when using materials that are not optimized for fabrication. For example, water-containing hydrogel scaffolds for biomedical applications often demand a complex 3D architecture with micron-scale features in order to capture the dynamic interactions between the cells and microenvironment, yet most hydrogel materials can hardly be fabricated at a very fine resolution (~ 1 um).

To achieve a high resolution in photopolymerization-based 3D printing, the proper light exposure dose must be determined. Insufficient exposure doses cannot photopolymerize the material, while excessive exposure doses can lead to polymerization beyond the desired regions. Generally, the proper exposure dose window is very narrow and needs to be identified for each desired structure and prepolymer material, which in practice is usually determined through manual

trial-and-error. This optimization process is time-consuming and costly, and often the resultant resolution achieved is suboptimal compared to both the desired designed dimensions and the printer's optical resolution.

This resolution deterioration is mainly caused by three factors, the first of which is light scattering. Optically-clear media allow for sharp patterns of high-fidelity, but the same patterns would be inevitably blurred or have suboptimal features in an optically-scattering media. The second factor is optical depth of focus—depending on the printing media, light can penetrate and polymerize up to a certain depth from the initial plane of incidence. If this penetration-and-polymerization thickness is greater than the optical depth of field, then the out-of-focus plane may experience unwanted polymerization. According to ray optics theory, an imaging system with a lens of numerical aperture of 0.05 and a resolution requirement of 5 μm will have a depth of focus of 100 μm. The polymerization thickness is determined by the absorption of the material, typically ranging from 100 μm to a few millimeters. [17,18] By doping the media with light absorbers, the polymerization thickness can be significantly reduced, minimizing resolution deterioration. The third is molecular diffusion, related to free-radical generation and propagation. Although free radicals are only generated within the light-illuminated region, free radicals and propagating chains can diffuse out of the light-illuminated areas and thus cause unwanted polymerization. According to Fick's laws of diffusion, the diffusion length can be estimated as $L = 2\sqrt{Dt}$, where D is the diffusivity and t is the free-radical lifetime,[19] where the diffusion coefficient of common free radicals are reported to be around 1 x 10^{-5} cm^{-2}/s in both polar and nonpolar solvents, [20,21] and free radical lifetimes has been reported to be at the scale of 10 milliseconds. [22] Thus, the free radical diffusion length is at the scale of a few microns, but by doping free radical quenchers, the diffusion length can be reduced. [6] These three factors may all be negligible in fabricating a

macro-scale device, yet they have substantial influence in microstructure fabrication or biological structure fabrication, where required feature sizes are on the order of microns as well. Among these three factors, light scattering represents a significant challenge, and can be difficult to mitigate since it is a material-dependent property.

Depending on the prepolymer's formulation and homogeneity, it may be optically clear prior to the start of fabrication, yet light scattering can increase as the material begins to polymerize. Some polymers, such as poly(methyl methacrylate) (PMMA), are as transparent as glass, thus barely suffer from the light scattering problem. Some others, notably hydrogels such as poly(ethylene glycol) diacrylate (PEGDA) hydrogel and di(ethylene glycol) dimethacrylate (DEGDMA) hydrogel, are initially a transparent liquid before polymerization, but once polymerized, they become translucent like agarose, signifying that they strongly scatter light.

Ideally, light exposure should be avoided as scattering increases, however current light-projection-based 3D printing techniques employ a continuous wave (CW) light source, such as a mercury lamp, laser, or light emitting diode (LED), to photopolymerize the prepolymer solution. With such CW sources, the light exposure, polymerization propagation, and increased scattering (opacification) all begin to overlap during the printing process, compounding the inevitability of scattering-induced photopolymerization of undesired regions, thus resulting in low print fidelity.

To address these challenges, we take advantage of how free-radical photopolymerization is a multi-step process, where light exposure conditions only affect free radical generation, [23,24] while the propagation of polymerizing chains can continue to take place even in dark conditions (i.e. after light illumination). Scherzer et. al. used real-time Fourier-transform infrared (FTIR) spectroscopy to investigate the photopolymerization process of tripropylene glycol diacrylate

(TPGDA) and found that chain propagation continues to proceed a few seconds after a short (~ 100 ms) and intense light exposure dose, eventually reaching a conversion rate similar to that when using a CW exposure.[25] Only a small fraction of the monomers in solution was consumed during the exposure period, while the majority was consumed during the dark period thereafter.

Here, we report a light-projection-based 3D printing system that uses flashing exposures for photopolymerization, henceforth referred to as flashing photopolymerization (FPP). With FPP, we chronologically separate three key events: light exposure, polymerization, and opacification. First, we apply a flashing exposure to generate a large amount of free radicals in the desired pattern; this is the light exposure step. Second, after light exposure has ceased, the prepolymer solution undergoes polymerization and opacification in the dark. In this way, the prepolymer is only exposed to light while it is negligibly scattering, thus minimizing scattering-induced resolution deterioration.

In this report, we first present the setup of the FPP 3D printer as well as examples of FPP-printed constructs. Next, we conducted resolution comparisons between CW and FPP and show how polymerization can increase scattering. Lastly, we model and simulate the photopolymerization process to explain the mechanism of FPP.

2. High fidelity 3D printing by flashing photopolymerization

The schematic of the FPP 3D printer is shown in Figure 1(a). The system uses a xenon flash tube as the light source, which is connected to an electronically-triggered controller unit. Using an optical lens setup, a digital micro-mirror device (DMD) projects the photomask image onto and through a transparent anti-adhesion substrate made of polydimethylsiloxane (PDMS, Sylgard 184, Dow Corning) coated on a glass vat containing the prepolymer solution. A motorized

stage is used to control the motion of the sample-supporting platform. Finally, a computer with custom software controls and synchronizes these mechanisms.

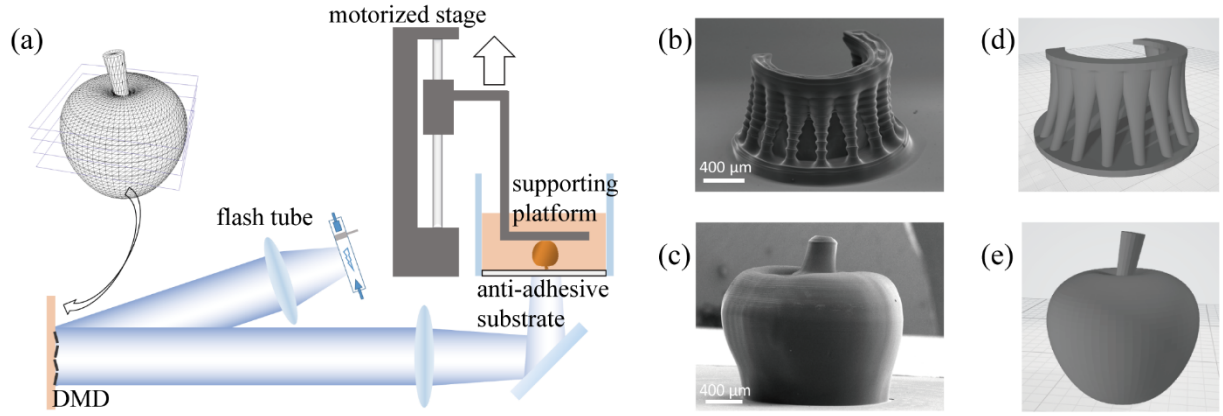

Figure 1. Flashing photopolymerization 3D printing. (a) Schematic of the FPP 3D printing system. (b) SEM image of a micro "altar" printed by FPP with 100 μm layer thickness. Scale bar = 400 μm. (c) SEM image of a micro "apple" printed by FPP with 20 μm layer thickness. Scale bar = 400 μm. (d) and (e) are the original 3D models of (b) and (c), respectively.

The 3D printing process is as follows: a digitally-designed 3D model is sliced into 2D cross-sectional images. The supporting platform is lowered to maintain a very narrow spacing (typically between 10 to 100 microns) between the supporting platform and the anti-adhesion substrate before printing. During printing, the xenon flash tube is triggered to flash at a specified energy; the resulting first layer photopolymerizes and attaches to the supporting platform. The motorized stage then raises the supporting platform by one layer thickness of typically 10-100 microns so that unpolymerized material can refill the subsequent vacant space between the anti-adhesion substrate and the previously-polymerized layer(s). A new 2D image slice can be loaded onto the DMD, and the flash tube flashes to solidify this new layer. By repeating these steps, a 3D object can be printed in a layer-by-layer manner.

In general, there is a tradeoff between print speed and quality, usually mediated by layer thickness. Printing with larger layer thicknesses allows for faster print times, albeit at the expense

of more inter-layer artifacts and a generally coarser quality, while printing with smaller layer thicknesses will produce better fabrication quality over a longer period of time. We demonstrate this with the 3D-printing of two representative structures using 100% PEGDA (Mn = 575 Da) and 4% (w/v) Irgacure 784, depicted in Figure 1. Figure 1(b) shows the scanning electron microscopy (SEM) image of an altar-like structure printed with a 100-µm-layer thickness, and Figure 1(c) shows the SEM image of an apple-like structure printed with 20-µm-layer thickness, which has a much smoother surface compared to the altar.

To compare the resolution differences between the FPP and CW printing modes, we designed a photomask with sharp, fine lines culminating in a spoke-like pattern. The photomask was printed on the same instrument using a UV-LED for CW and a xenon flash tube for FPP modes and with an aqueous hydrogel prepolymer solution containing 50% (v/v) PEGDA mixed with 4% (w/v) lithium phenyl-2,4,6-trimethylbenzoylphosphinate (LAP) as the photoinitiator. To simplify testing and analysis, we limited the printed structure to a single 250-µm thick layer, where different exposure doses were used to polymerize the structure. For the continuous UV-LED, we used a series of different energy outputs but kept the illumination time constant, whereas for the flash tube we used a series of different total energies but delivered in a single flash exposure for each. We evaluated resolution in this case by determining the unresolved fraction, that is, the ratio between the unresolved diameter and the outer diameter of the spoke-pattern. Here, a smaller unresolved fraction would mean a better resolution.

To calibrate the exposure dose, we used a series of different LED output powers and a series of different flash energies to polymerize a volume of prepolymer solution. At low exposure doses, the material is unable to polymerize, but as we increased the energy, at a certain value the spoke-pattern was able to polymerize – we defined this value as the minimum *unit exposure dose*.

Note that the unit exposure dose represents different energies in the CW vs. FPP modes as they are significantly different in both duration time and electromagnetic spectrum. From this, we defined a *relative exposure dose* E_r the ratio between the actual exposure energy and the unit exposure dose. We used E_r = {1, 1.26, 1.59, 2, 2.52, 3.18, 4} across both the CW and FPP modes to polymerize our spoke pattern structure and assess the unresolved fractions for each mode.

Figures 2(a) and 3(b) show bright-field microscopy images of the resultant structures for the CW exposure and FPP exposure modes, respectively. We noted two trends: 1) that the peripheral parts of the spoke pattern are often well-resolved due to their large relative spacing, while the centers are difficult to resolve due to their small relative spacing; and 2) that a higher total exposure dose leads to a larger unresolved area. The outer diameter of the spoke is 1.9 mm, and the unresolved diameter is less than 0.4 mm for all samples. The relation between the exposure energy and unresolved fraction is plotted in Figure 2(c). As can be seen from the plot, the FPP exposure mode always has a better resolution than that of the continuous mode. For the CW mode, it is clear that the unresolved fraction is strongly-dependent on the exposure dose, while for the FPP exposure mode, the unresolved fraction is insensitive to the exposure energy. When $E_r = 1$, the unresolved region resulting from FPP is 82% as large as that of when using CW. When $E_r = 4$, the unresolved region resulting from FPP is 23% as large as that of when using CW. These results show that using FPP can achieve better capability in resolving fine structures than using CW, and by using a flashing light source, the tolerance window of exposure dose is significantly broadened while simultaneously increasing fabrication resolution, thus significantly simplifying the optimization process.

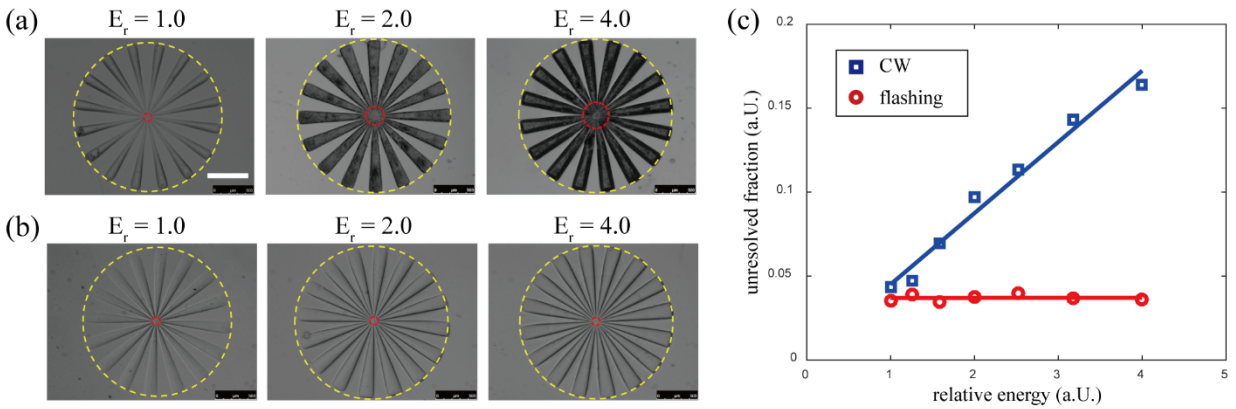

Figure 2. Resolution test for the CW exposure mode and FPP exposure mode. (a) Patterns printed with CW exposure at different relative energies. (b). Patterns printed with FPP exposure at different relative energies. (c) Relation between the relative energy and unresolved fraction. Yellow and red circles in (a) and (b) indicate the outer diameter and the unresolved diameter, respectively. Scale bar = 500 μm.

3. Theory and mechanism

3.1 Material scattering

Scattering is a significant factor in resolution deterioration and is known to be caused by molecular size, crystallinity, and phase separation. In a homogeneous polymer system, Rayleigh light scattering off the particles in the medium dominates, where the intensity is proportional to the molecular weight of the polymer.[23] For polymers that have semi-crystalline domains, their micron-size crystallites can induce strong Mie scattering.[26] Typically, a polymer has porous microstructures if it is polymerized from a monomer in solution because local solubility decreases as the polymer chain length increases. As polymerization continues, system homogeneity decreases as a result of phase separation, making it highly scattering.[27] In photopolymerization-based 3D printing, all three of these effects may occur and compound – light exposure induces molecular weight increase and thus Rayleigh scattering also increases. As the liquid-state prepolymer starts to solidify, crystallites also begin forming, thus causing further light scattering. In cases where the prepolymer contains solvents (e.g. hydrogels), the scattering phenomenon can

be even stronger due to the resultant phase separation. Altogether, opacification of the material leads to nonspecific exposure and polymerization in undesired areas, resulting in deteriorated fabrication resolution.

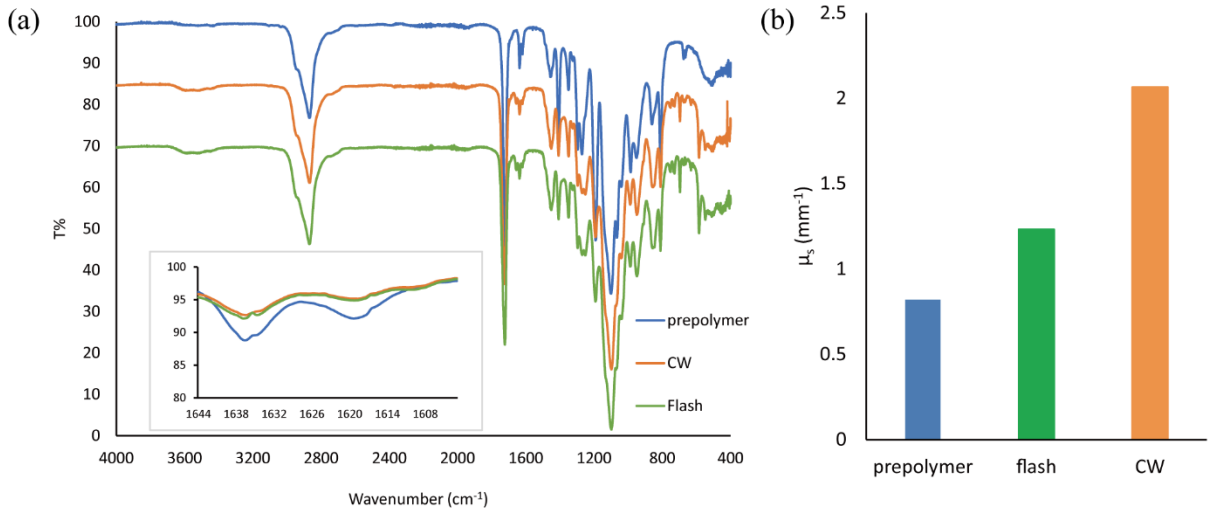

Figure. 3. Scattering changes during polymerization. (a) FTIR spectrum of pure PEGDA (Mn = 575), dehydrated PEGDA slab polymerized with FPP exposure, and dehydrated PEGDA slab polymerized by CW exposure. Inset: zoom-in view at around 1630 cm^{-1}. (b) Scattering coefficient of PEGDA prepolymer solution, PEGDA slab polymerized with FPP exposure, and PEGDA slab polymerized by CW exposure at 365 nm.

In order to demonstrate that the material opacifies as it polymerizes, we fabricated slab samples with 50% PEGDA and 4% LAP via both CW and FPP methods and measured their monomer conversion rates and scattering coefficients at 365 nm. A FTIR spectroscope was used to measure the infrared (IR) transmittance of the unpolymerized PEGDA, the slabs polymerized via CW, and the slabs polymerized via FPP, the results of which are shown in Figure 3(a). As compared to unpolymerized PEGDA, the alkene groups were consumed after exposure as shown in the reduction of absorption peak of C=C bond around 1630 cm^{-1}.[28,29] The conversion rate of PEGDA polymer after CW and FPP exposure was calculated to be 27.5% and 22.2%, respectively.

Separately, a UV-Vis-NIR spectroscope with integrating sphere was used to measure the scattering property of the same three sample types. The scattering coefficients were calculated with the Inverse Adding-Doubling (IAD) algorithm, which is widely used in calculating the scattering coefficient and absorption coefficient of thick biological tissue. [30,31] The scattering coefficients at 365 nm were calculated to be 0.82 mm^{-1}, 1.23 mm^{-1}, and 2.07 mm^{-1} for the prepolymer sample, slab polymerized via FPP, and slab polymerized via CW exposure, respectively (Figure 3(b)). This shows that as the PEGDA prepolymer undergoes photopolymerization either by CW or FPP exposure, its scattering coefficient increases. A high-speed camera was used to record this opacification in real-time to further validate the opacification phenomenon, shown in Figure S4.

3.2. Photopolymerization kinetics

Using FPP we can chronologically separate the light exposure event from downstream polymerization and opacification effects, the mechanism of which can be explained by photopolymerization kinetics. The free-radical photopolymerization process can be divided into three stages: 1) photoinitiation, where upon exposure to light, a photoinitiator molecule is homolytically-cleaved into two free radicals. These react with monomers and then become active propagating chains. 2) The second stage is propagation, where the initial chains continue to react with monomers and grow longer. 3) The third is termination, where an active chain stops propagating after combining with a free radical or another propagating chain.[32]

The initiation rate is proportional to the photoinitiator quantum yield Φ and photon absorption quantity per unit volume per unit time N_{abs}. The reaction rate of chain propagation r_p is proportional to reactive functional group concentration *[M]*, propagating chain concentration *[P*]*, and chain propagation rate coefficient k_p. The reaction rate of chain termination is proportional to

the square of propagating chain concentration *[P*]* and chain termination rate coefficient k_t. The initiation rate, propagation rate and termination rate are given by Equations (1)-(3). [23]

$$r_i = 2\Phi N_{abs} \tag{1}$$

$$r_p = k_p[M][P^*] \tag{2}$$

$$r_t = k_t[P^*]^2 \tag{3}$$

The change of reactive functional group concentration and propagating chain concentration are given by Equations (4), (5).

$$\frac{\partial[M]}{\partial t} = -r_p \tag{4}$$

$$\frac{\partial[P^*]}{\partial t} = r_i - r_t \tag{5}$$

As the prepolymer solution becomes more viscous, both the propagation kinetic constant and termination kinetic constant decrease during polymerization reaction. According to the well-established diffusion-controlled free-radical polymerization model,[28,33–37] the propagation rate coefficient k_p and the termination rate coefficient k_t can be determined by Equations (6) and (7), [28,37]

$$k_p = \frac{1}{\frac{1}{k_{p0}} + \frac{1}{k_{p,D}}} \tag{6}$$

$$k_t = \frac{1}{1/k_{t,SD} + 1/k_{t,TD}} + k_{t,RD} \tag{7}$$

where k_{p0} is the propagation rate coefficient without diffusion control; $k_{p,D}$ characterizes the diffusion-controlled part of the propagation reaction; $k_{t,SD}$ is the segmental-diffusion-controlled termination rate coefficient; $k_{t,TD}$ is the translational-diffusion-controlled termination rate coefficient; $k_{t,RD}$ is the reaction-diffusion-controlled termination rate coefficient. Additional equations and constants to model the photopolymerization process are available in the Experimental Section.

Here we use the model described above to numerically solve the photopolymerization kinetics problem in two scenarios. For both scenarios, the material system is 100% PEGDA with 4% (w/v) Irgacure 784 photoinitiator. Sample thickness is 100 microns. The photoinitiator has an absorbance A = 1.6 at 365 nm at 1 cm thickness at 0.1% concentration, thus A = 0.64 at 100 micron thickness at 4% concentration. We assume that the quantum efficiency of the photoinitiator is 1. In the first scenario, there is a low-intensity CW exposure lasting for 5 seconds. We simulated the photopolymerization kinetics under the light illumination intensity at 1.1 $mW \cdot cm^{-2}$, 2.2 $mW \cdot cm^{-2}$, or 4.3 $mW \cdot cm^{-2}$. In the second scenario, there is a flashing exposure, which lasts for 10 milliseconds. We simulated the average flashing intensity at 106.5 $W \cdot cm^{-2}$, 117.2 $W \cdot cm^{-2}$, or 127.8 $W \cdot cm^{-2}$. (See Table S1 for the relation between illumination intensity and free radical generation rate).

The simulation results are shown in Figure 4(a) and (b), respectively. The shaded area in Figure 4 indicates the light exposure period. The material properties and kinetic parameters of PEGDA have been studied previously [28] and are summarized in the Experimental Section.

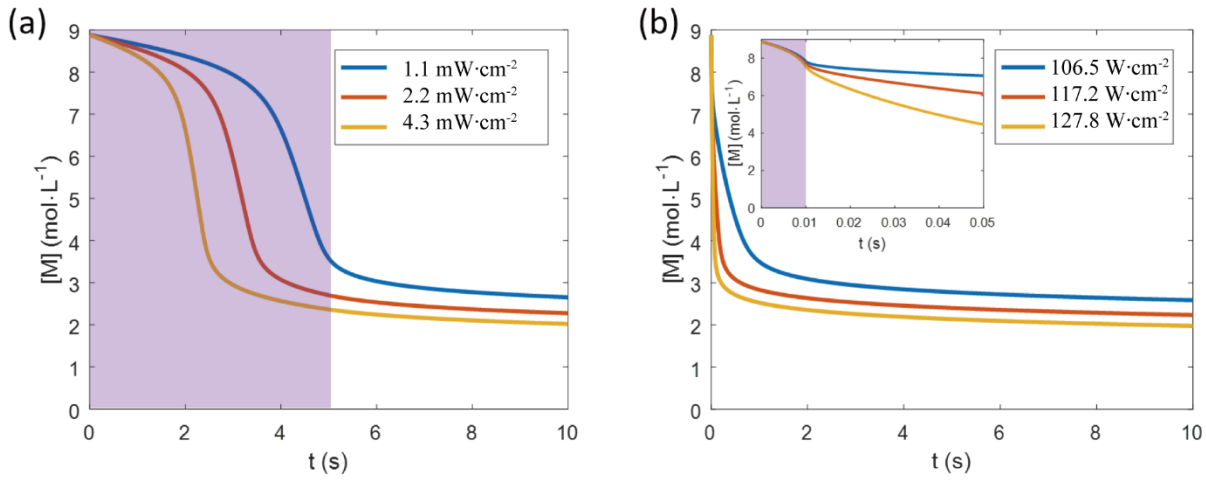

Figure 4. PEGDA photopolymerization simulation of the CW mode and the FPP mode. Unconverted reactive functional group concentration versus time. (a) The system is subject to a 5-second light exposure under the light illumination intensity at 1.1 mW·cm^{-2}, 2.2 mW·cm^{-2}, or 4.3 mW·cm^{-2}. (b) The system is subject to a 10-millisecond light exposure at 106.5 W·cm^{-2}, 117.2 W·cm^{-2}, or 127.8 W·cm^{-2}. The inset of (b) is a zoom-in view of the flash-exposure time region. The shaded area indicates the light exposure period.

From Figure 4, we can see that both scenarios reach a similar final conversion rate, showing that even a short exposure is sufficient to photopolymerize the monomer. The difference is that in the CW exposure scenario, polymerization and opacification begins and continues to occur while the light is still on, and the aforementioned scattering effects will send light outside of the desired areas. In the FPP scenario, the material can 'safely' polymerize and opacify in darkness, with no light to scatter into undesired areas.

4. Conclusion

We have successfully developed a flashing photopolymerization (FPP) method for photopolymerization-based 3D printing. By using a brief flash exposure instead of a continuous exposure, the material remains optically clear during the exposure period, thus minimizing light scattering and resulting in finer fabrication resolution. Both theoretical analysis and experimental demonstration have revealed the different scattering effects associated with CW vs. FPP exposure

modes. By chronologically separating the light exposure event from the polymerization and opacification events, one can significantly improve the fidelity of 3D-printed structures. This is particularly significant for microscale 3D printing where scattering effects can have significant impacts on the feature sizes necessary for microstructure formation, such as hydrogel 3D printing for bioengineering.

5. Experimental Section

Materials:

PEGDA (Mn = 575 Da) was purchased from Sigma-Aldrich. Irgacure 784 was purchased from Ciba Specialty Chemicals, now a subsidiary of BASF. LAP was synthesized in-house following previously-published methods.[38] The xenon flash tube was purchased from Xenon Flash Tubes.

Simulation of photopolymerization:

The propagation and termination kinetic of the system is related to the degree of conversion, as shown in Equations (8)-(12), [28,37]

$$X = ([M]_0 - [M]) / [M]_0 \tag{8}$$

$$k_{\mathrm{p},D} = \frac{k_{\mathrm{p},D0}}{e^{cX}} \tag{9}$$

$$k_{t,TD} = \frac{k_{t,TD0}}{e^{cX}} \tag{10}$$

$$k_{t,SD} = k_{t,SD0} \tag{11}$$

$$k_{t,RD} = C_{RD} k_p (1 - X) \tag{12}$$

where X is the degree of conversion; $[M]$ is the unconverted functional group (C=C double bond) concentration, $[M]_0$ is the initial unconverted functional group concentration; c is the relative viscosity coefficient; $k_{p,D0}$ is the diffusion-controlled propagation rate coefficient at zero conversion; $k_{t,TD0}$ and $k_{t,SD0}$ are the translational-diffusion-controlled termination rate coefficient and the segmental-diffusion-controlled termination rate coefficient at zero conversion; C_{RD} is the reaction-diffusion proportion parameter.

The material properties and kinetic parameters of PEGDA (Mn = 250) are listed in Table 1. [28] MATLAB (The MathWorks, Inc., Natick, MA) was used to perform the numerical simulation.

Table 1. Material properties and kinetic parameters of PEGDA

$[M_0]$	8.88 mol·L^{-1}	c	34.149
k_{p0}	1860 L·mol^{-1}·s^{-1}	$k_{p,D0}$	8.994 x 10^{11} L·mol^{-1}·s^{-1}
$k_{t,SD}$	4.39 x 10^{6} L·mol^{-1}·s^{-1}	$k_{t,TD0}$	1.002 x 10^{7} L·mol^{-1}·s^{-1}
C_{RD}	1.0146		

Infrared spectrum measurement:

IR spectrum measurements were performed on a Perkin Elmer Spectrum Two FTIR spectroscope. Polymerized samples were dried to eliminate the influence of the spectrum of water; first by snap-freeze in liquid nitrogen, then dried by lyophilization (Labconco Freezone, lyophilize at -55 °C for 3 days).

Scattering coefficient measurement:

Three samples were prepared for the measurement in a UV-Vis-NIR spectroscope (Perkin Elmer, Lambda 1050). The prepolymer solution (50% PEGDA, 4% LAP) is loaded in a 1 mm wide glass container. The FPP sample is polymerized by a single flash (20 J) into a 1 mm slab. The CW sample is polymerized by UV-LED (0.4 mW cm^{-2}, 10 s) into a 1 mm slab.

By using the integrating sphere, the diffusive reflectance R_d, total reflectance R_t, diffusive transmittance T_d, and total transmittance T_t at 365 nm wavelength are measured. Then we used Inverse Adding-Doubling (IAD) algorithm to calculate the scattering coefficient of the samples. The executable program of IAD algorithm was acquired from https://omlc.org/software/iad/index.html, copyright 2017 Scott Prahl.

ACKNOWLEDGMENT

This work was supported in part by National Institutes of Health (R21AR074763, R33HD090662, and R01EB021857) and National Science Foundation (NSF) (CMMI-1644967). Part of the work is performed at San Diego Nanotechnology Infrastructure (SDNI) of UCSD, a member of the National Nanotechnology Coordinated Infrastructure (NNCI), which is supported by NSF (Grant ECCS-1542148). This material is based upon work supported by the National Science Foundation Graduate Research Fellowship Program under Grant No. DGE-1650112 to JS.

REFERENCES

[1] J.R. Tumbleston, D. Shirvanyants, N. Ermoshkin, R. Janusziewicz, A.R. Johnson, D. Kelly, K. Chen, R. Pinschmidt, J.P. Rolland, A. Ermoshkin, E.T. Samulski, J.M. DeSimone, Continuous liquid interface production of 3D objects, Science. 347 (2015) 1349–1352. doi:10.1126/science.aaa2397.

[2] C. Sun, N. Fang, D.M. Wu, X. Zhang, Projection micro-stereolithography using digital micro-mirror dynamic mask, Sensors and Actuators A: Physical. 121 (2005) 113–120. doi:10.1016/j.sna.2004.12.011.

[3] R. Gauvin, Y.-C. Chen, J.W. Lee, P. Soman, P. Zorlutuna, J.W. Nichol, H. Bae, S. Chen, A. Khademhosseini, Microfabrication of complex porous tissue engineering scaffolds using 3D projection stereolithography, Biomaterials. 33 (2012) 3824–3834. doi:10.1016/j.biomaterials.2012.01.048.

[4] L.-H. Han, J.A. Easley, C.J. Ellison, S. Chen, Fluorinated Colloidal Emulsion of Photochangeable Rheological Behavior as a Sacrificial Agent to Fabricate Organic, Three-Dimensional Microstructures, Langmuir. 26 (2010) 6108–6110. doi:10.1021/la100014k.

[5] P. Soman, B.T.D. Tobe, J.W. Lee, A.A.M. Winquist, I. Singec, K.S. Vecchio, E.Y. Snyder, S. Chen, Three-dimensional scaffolding to investigate neuronal derivatives of human embryonic stem cells, Biomedical Microdevices. 14 (2012) 829–838. doi:10.1007/s10544-012-9662-7.

[6] A.P. Zhang, X. Qu, P. Soman, K.C. Hribar, J.W. Lee, S. Chen, S. He, Rapid Fabrication of Complex 3D Extracellular Microenvironments by Dynamic Optical Projection Stereolithography, Advanced Materials. 24 (2012) 4266–4270. doi:10.1002/adma.201202024.

[7] W. Zhu, X. Ma, M. Gou, D. Mei, K. Zhang, S. Chen, 3D printing of functional biomaterials for tissue engineering, Current Opinion in Biotechnology. 40 (2016) 103–112.

[8] W. Zhu, K.R. Tringale, S.A. Woller, S. You, S. Johnson, H. Shen, J. Schimelman, M. Whitney, J. Steinauer, W. Xu, Rapid continuous 3D printing of customizable peripheral nerve guidance conduits, Materials Today. (2018).

[9] D.B. Berry, S. You, J. Warner, L.R. Frank, S. Chen, S.R. Ward, A 3D tissue-printing approach for validation of diffusion tensor imaging in skeletal muscle, Tissue Engineering Part A. 23 (2017) 980–988.

[10] W. Zhu, X. Qu, J. Zhu, X. Ma, S. Patel, J. Liu, P. Wang, C.S.E. Lai, M. Gou, Y. Xu, K. Zhang, S. Chen, Direct 3D bioprinting of prevascularized tissue constructs with complex microarchitecture, Biomaterials. 124 (2017) 106–115. doi:10.1016/j.biomaterials.2017.01.042.

[11] X. Qu, W. Zhu, S. Huang, Y.-S. Li, S. Chien, K. Zhang, S. Chen, Relative impact of uniaxial alignment vs. form-induced stress on differentiation of human adipose derived stem cells, Biomaterials. 34 (2013) 9812–9818. doi:10.1016/j.biomaterials.2013.09.009.

[12] J.-F. Xing, M.-L. Zheng, X.-M. Duan, Two-photon polymerization microfabrication of hydrogels: an advanced 3D printing technology for tissue engineering and drug delivery, Chemical Society Reviews. 44 (2015) 5031–5039. doi:10.1039/C5CS00278H.

[13] P. Soman, D.Y. Fozdar, J.W. Lee, A. Phadke, S. Varghese, S. Chen, A three-dimensional polymer scaffolding material exhibiting a zero Poisson's ratio, Soft Matter. 8 (2012) 4946. doi:10.1039/c2sm07354d.

[14] H.N. Chia, B.M. Wu, Recent advances in 3D printing of biomaterials, Journal of Biological Engineering. 9 (2015) 4. doi:10.1186/s13036-015-0001-4.
[15] T.E. Brown, K.S. Anseth, Spatiotemporal hydrogel biomaterials for regenerative medicine, Chemical Society Reviews. 46 (2017) 6532–6552. doi:10.1039/C7CS00445A.
[16] P. Soman, J.W. Lee, A. Phadke, S. Varghese, S. Chen, Spatial tuning of negative and positive Poisson's ratio in a multi-layer scaffold, Acta Biomaterialia. 8 (2012) 2587–2594.
[17] A. del Campo, C. Greiner, SU-8: a photoresist for high-aspect-ratio and 3D submicron lithography, Journal of Micromechanics and Microengineering. 17 (2007) R81–R95. doi:10.1088/0960-1317/17/6/R01.
[18] S. You, W. Zhu, P. Wang, S. Chen, Projection Printing of Ultrathin Structures with Nanoscale Thickness Control, ACS Applied Materials & Interfaces. 11 (2019) 16059–16064. doi:10.1021/acsami.9b02728.
[19] R.B. Bird, W.E. Stewart, E.N. Lightfoot, Transport phenomena, John Wiley & Sons, 2007.
[20] M. Terazima, Y. Nogami, T. Tominaga, Diffusion of a radical from an initiator of a free radical polymerization: a radical from AIBN, Chemical Physics Letters. 332 (2000) 503–507. doi:10.1016/S0009-2614(00)01298-7.
[21] R.L. Donkers, D.G. Leaist, Diffusion of Free Radicals in Solution. TEMPO, Diphenylpicrylhydrazyl, and Nitrosodisulfonate, The Journal of Physical Chemistry B. 101 (1997) 304–308. doi:10.1021/jp961957k.
[22] W. Reed, L. Guterman, P. Tundo, J.H. Fendler, Polymerized surfactant vesicles: kinetics and mechanism of photopolymerization, Journal of the American Chemical Society. 106 (1984) 1897–1907. doi:10.1021/ja00319a001.
[23] C.E. Carraher Jr, Introduction to polymer chemistry, CRC press, 2017.
[24] J.M.G. Cowie, V. Arrighi, Polymers: chemistry and physics of modern materials, CRC press, 2007.
[25] T. Scherzer, U. Decker, Real-time FTIR–ATR spectroscopy to study the kinetics of ultrafast photopolymerization reactions induced by monochromatic UV light, Vibrational Spectroscopy. 19 (1999) 385–398.
[26] J.-C. Auger, R.G. Barrera, B. Stout, Scattering efficiency of clusters composed by aggregated spheres, Journal of Quantitative Spectroscopy and Radiative Transfer. 79–80 (2003) 521–531. doi:10.1016/S0022-4073(02)00305-9.
[27] A. Seeboth, D. Lötzsch, E. Potechius, Phase transitions and phase separations in aqueous polyether systems, Colloid Polym Sci. 279 (2001) 696–704. doi:10.1007/s003960000474.
[28] J. Wu, Z. Zhao, C.M. Hamel, X. Mu, X. Kuang, Z. Guo, H.J. Qi, Evolution of material properties during free radical photopolymerization, Journal of the Mechanics and Physics of Solids. 112 (2018) 25–49. doi:10.1016/j.jmps.2017.11.018.
[29] Y.-H. Hsueh, W.-C. Liaw, J.-M. Kuo, C.-S. Deng, C.-H. Wu, Hydrogel Film-Immobilized Lactobacillus brevis RK03 for γ-Aminobutyric Acid Production, International Journal of Molecular Sciences. 18 (2017) 2324. doi:10.3390/ijms18112324.
[30] M. Mesradi, A. Genoux, V. Cuplov, D. Abi Haidar, S. Jan, I. Buvat, F. Pain, Experimental and analytical comparative study of optical coefficient of fresh and frozen rat tissues, Journal of Biomedical Optics. 18 (2013) 117010. doi:10.1117/1.JBO.18.11.117010.
[31] S.A. Prahl, M.J.C. van Gemert, A.J. Welch, Determining the optical properties of turbid media by using the adding–doubling method, Applied Optics. 32 (1993) 559. doi:10.1364/AO.32.000559.

[32] C.N. Bowman, C.J. Kloxin, Toward an enhanced understanding and implementation of photopolymerization reactions, AIChE Journal. 54 (2008) 2775–2795. doi:10.1002/aic.11678.
[33] M.D. Goodner, H.R. Lee, C.N. Bowman, Method for determining the kinetic parameters in diffusion-controlled free-radical homopolymerizations, Industrial & Engineering Chemistry Research. 36 (1997) 1247–1252.
[34] M.D. Goodner, C.N. Bowman, Modeling primary radical termination and its effects on autoacceleration in photopolymerization kinetics, Macromolecules. 32 (1999) 6552–6559.
[35] M.R. Gleeson, J.T. Sheridan, Nonlocal photopolymerization kinetics including multiple termination mechanisms and dark reactions Part I Modeling, Journal of the Optical Society of America B. 26 (2009) 1736. doi:10.1364/JOSAB.26.001736.
[36] M.D. Goodner, C.N. Bowman, Development of a comprehensive free radical photopolymerization model incorporating heat and mass transfer effects in thick films, Chemical Engineering Science. 57 (2002) 887–900. doi:10.1016/S0009-2509(01)00287-1.
[37] M. Buback, Free-radical polymerization up to high conversion. A general kinetic treatment, Die Makromolekulare Chemie. 191 (1990) 1575–1587. doi:10.1002/macp.1990.021910710.
[38] B.D. Fairbanks, M.P. Schwartz, C.N. Bowman, K.S. Anseth, Photoinitiated polymerization of PEG-diacrylate with lithium phenyl-2,4,6-trimethylbenzoylphosphinate: polymerization rate and cytocompatibility, Biomaterials. 30 (2009) 6702–6707. doi:10.1016/j.biomaterials.2009.08.055.

Supplementary Information

Figure S1 shows closeup views of the images in Figure 2. Visual observation makes it clear that the fabrication resolution of the CW mode decreases as exposure dose increases. By comparison, the FPP mode can maintain fine resolution even at excessive exposure doses.

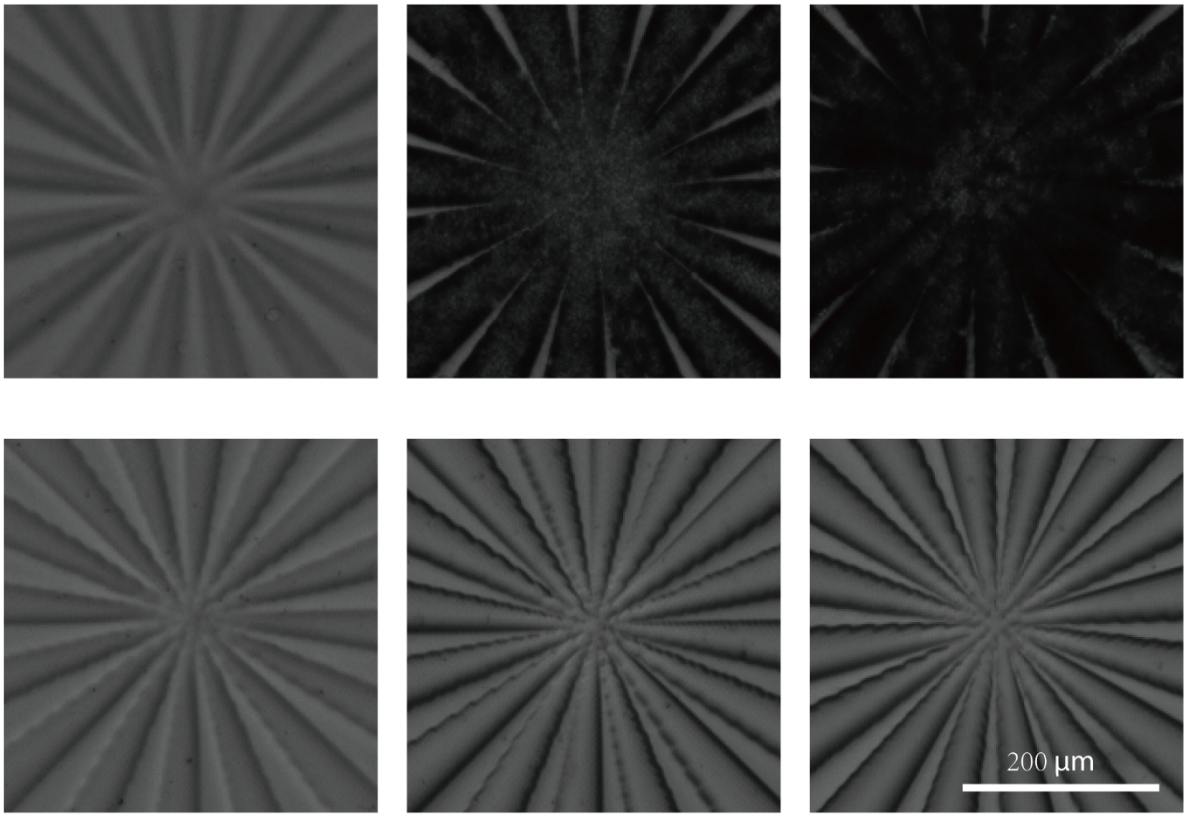

Figure S1. Zoom-in view of images in Figure 2. First row: patterns printed with CW exposure.

Second row: patterns printed with FPP.

The slab samples for scattering measurement in Figure 3 have different visual appearances. The CW sample is much more opaque than the FPP sample. Figure S2 shows the appearance of the two samples.

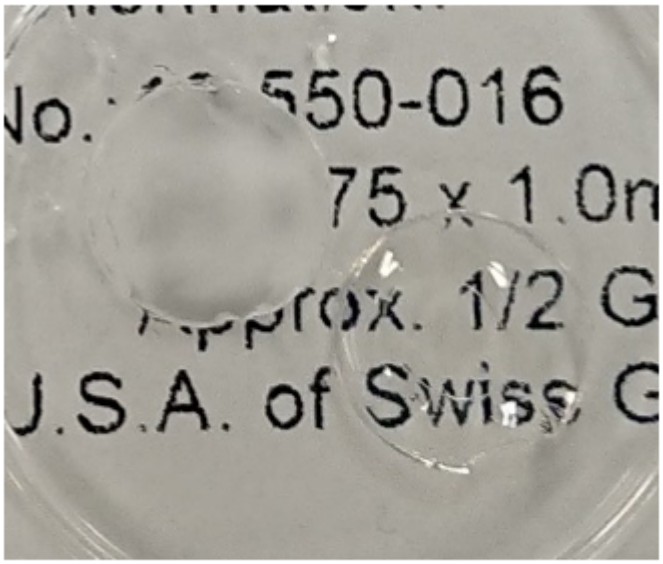

Figure S2. Appearance of the slab samples. The upper-left disc is made by CW exposure, and the lower-right disc is made by FPP exposure

In order to visualize the opacification during photopolymerization in real-time, a high-speed camera was used to record the change of Tyndall effect on a photopolymerizable material. The material is aqueous 50% (v/v) PEGDA with 4% (w/v) LAP added as the photoinitiator. The prepolymer solution was loaded in a cuvette, and a He-Ne laser beam (633 nm) was shone through the solution such that the beam path and its shape was visible to the high-speed camera (Figure S3). Finally, either a UV-LED light source (365 nm) or a xenon flash tube was set up near the cuvette to photopolymerize the PEGDA solution.

The UV-LED was record to have a light intensity of 12 mW cm^{-2} at the cuvette. The xenon flash tube has a broad emission spectrum encompassing from UV to NIR, with an electrical energy per flash of 40 J. However, we did not have a suitable instrument to measure the actual light intensity of the flash illumination at the cuvette. The high-speed camera was set to record at 500 fps, with a 2 ms exposure time for each frame. The image was recorded at monochromatic 16-bit

bit-depth, and the gray scale value ranged from 0 to 65535. The original recorded grey scale value was used as the intensity in Figure S4 (b) and (d). The beginning and ending time of exposure was determined based on the subtle change of background brightness, since the long pass filter does not completely block the light from the LED or flash tube.

We used either a 2.3-second CW exposure from the UV-LED or a single flashing exposure from the xenon flash tube to polymerize the prepolymer solution. The change of shape of the laser beam inside the PEGDA was recorded, as shown in Figure S4(a) for CW exposure and in Figure S4(c) for FPP exposure. The intensity profiles along the green arrows were plotted in Figure S4(b) for CW exposure and in Figure S4(d) for FPP exposure.

As was expected, light scattering increased during photopolymerization in both cases. In the CW exposure case, scattering steadily increases during the 2.3-second exposure, and at the end of exposure period the material is highly scattering, with scattering still continuing to increase even after the exposure period. In the FPP exposure case, the first 50 milliseconds of the recorded video was strongly interfered with by the intense flashing, and laser beam shape was unable to be observed, but at the end of the flash (t = 50 ms), the material scattering has increased only slightly. The scattering keeps increasing in the next several hundreds of milliseconds.

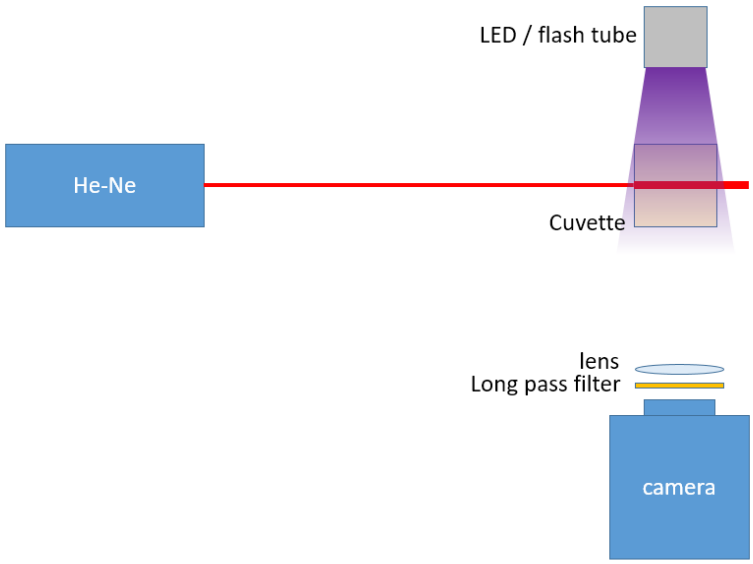

Figure S3. Optical setup for visualizing the opacification during polymerization.

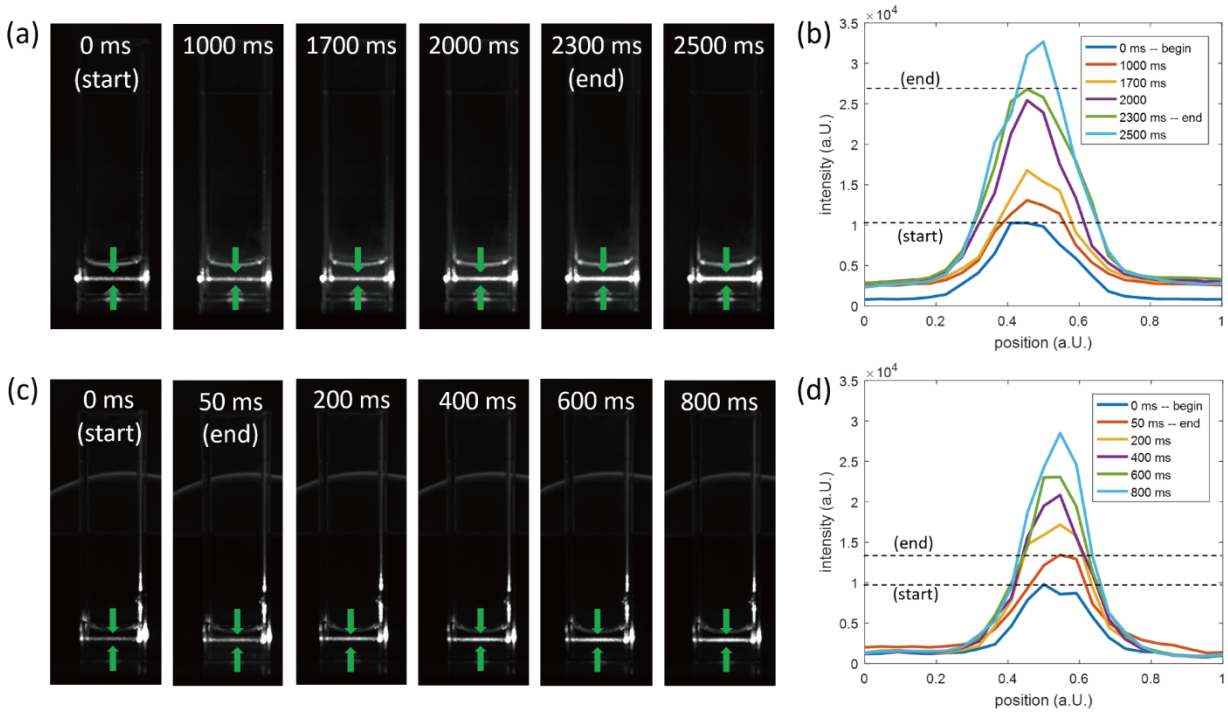

Figure S4. Scattering changes during polymerization. (a) Images of Tyndall effect at different time point of CW exposure. (b) Intensity profile of the laser beam along the green arrows in (a). (c) Images of Tyndall effect at different time points of FPP exposure. (d) Intensity profile of the laser beam along the green arrows in (c).

In the simulation, the type and concentration of photoinitiator, and the illumination intensity are given, thus the free radical generation rate can be calculated, then the kinetics simulation can be performed with Equations (1) – (11). Here is the method to convert the illumination intensity into free-radical generation rate.

The free radical generation rate r_i is proportional to the quantity of photons absorbed per unit time per unit volume N_{abs}, and to the quantum efficiency Φ:

$$r_i = 2\Phi N_{abs} \tag{S1}$$

According to Beer-Lambert law, the molar quantity of photons absorbed, N_{abs} per unit volume is related to the material absorbance A, light power intensity I, sample thickness L, and photon frequency ν:

$$N_{abs} = (1 - 10^{-A}) \cdot \frac{I}{N_A h\nu} \cdot \frac{1}{L} \tag{S2}$$

where N_A and h are Avogadro constant and Plank constant.

The material absorbance A is determined by the molar extinction coefficient ε, the photoinitiator concentration C (neglecting monomer absorption), and the sample thickness L.

$$A = \frac{\varepsilon C L}{\ln(10)} \tag{S3}$$

Combining Equations (S1) – (S3), the free radical generation rates at different illumination intensities can be calculated. Table S1 lists the corresponding free radical generation rates associated with the light illumination intensities used in the simulation.

Table S1. Free radical generation rates and corresponding illumination intensity.

Free Radical Generation Rate	Light Intensity
0.0005 mol L^{-1} s^{-1}	1.1 mW cm^{-2}
0.001 mol L^{-1} s^{-1}	2.2 mW cm^{-2}
0.002 mol L^{-1} s^{-1}	4.3 mW cm^{-2}
50 mol L^{-1} s^{-1}	106.5 W cm^{-2}
55 mol L^{-1} s^{-1}	117.2 W cm^{-2}
60 mol L^{-1} s^{-1}	127.8 W cm^{-2}